RAA 2021 Vol. **21** No. **3**, 71(10pp) doi: 10.1088/1674-4527/21/3/71

http://www.raa-journal.org *http://iopscience.iop.org/raa*

***R**esearch in*
***A**stronomy and*
***A**strophysics*

Chaos-induced resistivity in different magnetic configurations

Zhen Wang (王桢)[1,2], De-Jin Wu (吴德金)[1], Ling Chen (陈玲)[1] and Yu-Fei Hao (郝宇飞)[1]

[1] Key Laboratory of Planetary Sciences, Purple Mountain Observatory, Chinese Academy of Sciences, Nanjing 210023, China; *djwu@pmo.ac.cn*

[2] University of Science and Technology of China, Hefei 230026, China

Received 2020 August 29; accepted 2020 September 19

Abstract It is widely believed that magnetic reconnection plays an important role in various eruptive phenomena of space and astrophysical plasmas. The mechanism of anomalous resistivity, however, has been an open and unsolved problem. The chaos-induced resistivity proposed by Yoshida et al. is one of possible mechanisms for anomalous resistivity. By use of the test particle simulation, the present work studies the chaos-induced resistivity for different configurations of reconnection magnetic fields and its distribution in different chaos regions of reconnection current sheets. The results show that the chaos-induced resistivity can be $6-7$ orders of magnitude higher than the classical Spitzer resistivity in the X-type chaos regions and 5 orders of magnitude in the O-type chaos regions. Moreover, in the X-type chaos regions the chaos-induced resistivity of the magnetized case is higher by a factor of 2 to 3 times than that of the unmagnetized case, but in the O-type chaos regions the chaos-induced resistivity of the magnetized case is close to or lower than that of the unmagnetized case. The present work is helpful to the understanding of the dynamics of reconnection current sheets, especially of the generation mechanism of the anomalous resistivity of collisionless reconnection regions.

Key words: magnetic fields — methods: numerical — plasmas — Sun: flares

1 INTRODUCTION

The early concept of magnetic reconnection was proposed by Giovanelli in 1946 to explain energy release in solar flares (Giovanelli 1946). Nowadays it has been extensively believed that the magnetic reconnection is one of the most effective processes of magnetic energy releasing in various eruptive phenomena (Ma et al. 2018; Lu et al. 2018), such as terrestrial aurora (Dungey 1961; McPherron 1979), solar flares (Parker 1957), γ-ray bursts (Lyutikov 2006) and the instability in fusion devices (Furth et al. 1963). The magnetic reconnection process reconfigures the magnetic field topology and converts the magnetic energy into the kinetic energy of the plasma particles via the heating or acceleration (Dungey 1953). This indicates the breaking of the frozen-in condition, which requires a high enough plasma resistivity much larger than the classical Coulomb collision resistivity (i.e., the so-called Spitzer resistivity) in the cases of solar flares and terrestrial aurora (Spitzer 1956; Cai & Lee 1997). Therefore a collisionless resistivity, usually called the anomalous resistivity or effective resistivity, is necessary for the collisionless magnetic reconnection (Ma et al. 2018).

Many different mechanisms have been proposed to be responsible for the generation of anomalous resistivity. For example, Huba et al. (1980) pointed out that lower-hybrid drift waves driven by the diamagnetic current can possibly contribute to the generation of the anomalous resistivity in an inhomogeneous plasma, Bulanov et al. (1992) showed that the electron magnetohydrodynamics effect may lead to the formation of the anomalous resistivity, and Biskamp et al. (1995) proposed that the Hall effect caused due to the finite ion inertia also is one of possible mechanisms for the anomalous resistivity. In addition, the presence of the MHD turbulence, which consists of stochastic magnetic fields over a wide scale range in the MHD inertial-scale region, may cause an "effective" reconnection of the stochastic magnetic fields, called the turbulent reconnection (Strauss 1988; Lazarian & Vishniac 1999; Lazarian et al. 2020). In this scenario, however, the so-called turbulent reconnection does not lead to the real dissipation of the energy in the inertial region, but merely the transport of the energy from larger to smaller scales due to the turbulent cascade process in the inertial region, and ultimately to the kinetic scales (Kim & Diamond 2001).

Some investigations of laboratory experiments and kinetic simulations also showed that in the kinetic scales

the small-scale turbulent magnetic fields typically have two-dimensional current sheet or three-dimensional flux rope structures (Gekelman et al. 2011; Liu et al. 2013). The real dissipation does occur at the kinetic scales of particles in a plasma, at which the motion of individual particles plays an important role. The kinetic mechanism of producing the anomalous resistivity that has been investigated most widely is the wave-particle interaction of turbulent plasma waves in the kinetic scales, such as ion-acoustic turbulence (Bychenkov et al. 1988), kinetic Alfvén waves (Voitenko 1995; Singh & Subramanian 2007), lower-hybrid waves (Carter et al. 2002), and whistler waves (Deng & Matsumoto 2001).

In fact, the physical nature of the anomalous resistivity is the randomization of the directional motion of the current-carrying charged particles in the reconnection current sheet. It had been recognized for a long time that in the neighborhood of the magnetic neutral point of a spatially inhomogeneous magnetic field, the orbital motion of charged particles possibly becomes a chaotic motion due to the strong gradient nonlinearity (Grad & Norton 1962; Schmidt 1962). Yoshida et al. (1998) pointed out that the chaotic motion of charged particles may be equivalent to the randomization (or i.e., thermalization) process of the directional motion of the current-carrying particles and hence also can contribute to the generation mechanism of the anomalous resistivity in the case of collisionless magnetic reconnection. Numata & Yoshida (2002, 2003) further investigated the anomalous resistivity caused by the chaotic motion of particles in an open system with the convection of particles into and out of the reconnection region. Their results showed that the continuous dissipation can be carried out and the resulting chaos-induced resistivity may reasonably explain the necessary anomalous resistivity leading to a fast magnetic reconnection.

However, in many realistic space and astrophysical plasma environments a mean magnetic field at a given scale frequently exists instead of a three-dimensional magnetic neutral point (i.e., a real magnetic null point). This indicates that the major magnetic reconnections are only partly magnetic reconnections with a nonzero guide magnetic field and the so-called magnetic neutral point actually is a two-dimensional X-type magnetic neutral point in the reconnection plane perpendicular to the guide field. Shang et al. (2017) generalized the works of Numata & Yoshida (2002, 2003) to the case with a guide field and found that the presence of a guide field can significantly influences the chaos-induced resistivity nearby the X-type magnetic neutral point and leads to the chaos-induced resistivity reaching its peak value when the guide field approaches half of the characteristic strength of the reconnection magnetic field.

Of course, actual configurations of reconnection magnetic fields in space and astrophysical plasmas usually are very complex and diverse and the most common one of them is small-scale current sheets, which may be produced by local plasma currents due to ubiquitous turbulent magnetic fields (Strauss 1988; Lazarian & Vishniac 1999; Gekelman et al. 2011; Liu et al. 2013; Lazarian et al. 2020). In this paper we extend the previous works (Shang et al. 2017) to the case of reconnection current sheets, in which there is a finite width magnetic neutral current sheet between two Y-type magnetic neutral points. In particular, the distribution of the chaos-induced resistivity in the reconnection current sheet is investigated and compared to the case of the magnetic configuration with a single X-type magnetic neutral point. The results show that the chaos-induced resistivity tends to concentrate in the neighborhood of the X- or Y-type neutral points, where the motion of particles gets into a chaotic orbit more easily. The possibility of application to the anomalous resistivity of magnetic reconnection in solar flaring plasmas is discussed. The present results are helpful to our understanding of the magnetic reconnection physics, especially to the generation mechanism of the anomalous resistivity in the collisionless magnetic reconnection.

The remains of this paper are organized as follows. The basic physics model and method used in this investigation are described in Section 2, then the results and discussion are presented in Section 3, and finally Section 4 is devoted to the summary and conclusions.

2 BASIC PHYSICS MODEL AND METHOD

The main aim of this work is to compare the chaos-induced resistivity in different magnetic configurations of reconnection fields. For the sake of convenience, we use a magnetic field model with three Cartesian rectangular components, $\boldsymbol{B} = (B_x,\ B_y,\ B_z)$, as follows:

$$\boldsymbol{B} = \begin{cases} \left[\tanh\left(\frac{y}{R_0}\right), \tanh\left(\frac{x}{R_0} - \frac{l}{2}\right), \delta\right] B_0, & x \geq \left(\frac{l}{2}\right) R_0 \\ \left[\tanh\left(\frac{y}{R_0}\right), \tanh\left(\frac{x}{R_0} + \frac{l}{2}\right), \delta\right] B_0, & x \leq -\left(\frac{l}{2}\right) R_0 \\ \left[\tanh\left(\frac{y}{R_0}\right), 0, \delta\right] B_0, & |x| < \left(\frac{l}{2}\right) R_0 \end{cases}, \tag{1}$$

where the components in $x - y$ plane, B_x and B_y, is the reconnection field, the component along the z axis, B_z, is the uniform guide field, B_0 and R_0 are the characteristic strength and the characteristic gradient scale of the reconnection magnetic field, respectively, δ is the relative strength of the guide field in units of B_0, and l is the relative width of the neutral current sheet in units of R_0. When $l = 0$, the reconnection field has the X-type magnetic configuration and when $l \to \infty$, the reconnection field becomes a one-dimensional Harris current sheet. For a finite $0 < l < \infty$, the reconnection field describes a neutral current sheet with a finite width of lR_0 between

the two Y-type magnetic neutral points, called the double Y-type magnetic configuration.

In addition, a constant acceleration electric field along the guide magnetic field is used, which is given by

$$\boldsymbol{E} = (0,\ 0,\ M_A)\, v_A B_0, \tag{2}$$

where M_A is the relative strength of the acceleration electric field E_z in units of $v_A B_0$ and v_A is the Alfvén velocity. Thus, in the collisionless condition (i.e., to neglect the interactions among particles), the motion equations of individual charged particles can be described as

$$\begin{aligned} \frac{\mathrm{d}\boldsymbol{r}}{\mathrm{d}t} &= \boldsymbol{v}, \\ \frac{\mathrm{d}\boldsymbol{v}}{\mathrm{d}t} &= \frac{q}{m}(\boldsymbol{E} + \boldsymbol{v} \times \boldsymbol{B}), \end{aligned} \tag{3}$$

where $\boldsymbol{B}$ and $\boldsymbol{E}$ are the magnetic and electric filed in Equations (1) and (2), respectively.

For convenience used in the numerical simulation, we introduce normalized variables as follows:

$$\begin{aligned} &\boldsymbol{r}' = \boldsymbol{r}/R_0,\ t' = t/\tau_A,\ \tau_A = R_0/v_A \\ &\boldsymbol{v}' = \boldsymbol{v}/v_A,\ E_z' = E_z/v_A B_0 = M_A,\ \boldsymbol{B}' = \boldsymbol{B}/B_0, \end{aligned} \tag{4}$$

where the variables with the superscript "′" are the dimensionless forms of the corresponding variables. Thus, the dimensionless forms of the electric and magnetic fields given by Equations (2) and (1) may be written as follows:

$$\boldsymbol{E}' = (0,\ 0,\ M_A) \tag{5}$$

and

$$\boldsymbol{B}' = \begin{cases} [\tanh(y'),\ \tanh(x' - l/2),\ \delta], & x' \geq l/2 \\ [\tanh(y'),\ \tanh(x' + l/2),\ \delta], & x' \leq -l/2, \\ [\tanh(y'),\ 0,\ \delta], & |x'| < l/2 \end{cases} \tag{6}$$

respectively. In particular, the dimensionless form of the motion Equation (3) can reduce to

$$\begin{aligned} \frac{\mathrm{d}\boldsymbol{r}'}{\mathrm{d}t'} &= \boldsymbol{v}', \\ \frac{\mathrm{d}\boldsymbol{v}'}{\mathrm{d}t'} &= \omega_c \tau_A \left(M_A + \boldsymbol{v}' \times \boldsymbol{B}'\right). \end{aligned} \tag{7}$$

In order to emphasize the effect of dynamical chaos of particle orbits, we take $R_0 = \lambda_c = v_A/\omega_c$, which implies $\omega_c \tau_A = 1$.

Following Numata & Yoshida (2003), Andriyas & Spencer (2014), and Shang et al. (2017), the anomalous resistivity due to the chaotic motion of particles may be calculated from the "average" acceleration of particles along the acceleration electric field, α, and the relative escape rate of particles from the chaos region, β, which are defined by the following expressions

$$\bar{v}_z'(t') = \alpha t' \tag{8}$$

and

$$n(t') = n_0 \exp(-\beta t'), \tag{9}$$

respectively, where $\bar{v}_z'(t')$ and $n(t')$ are the "average" velocity and number density of accelerated particles in the chaos region, respectively. For a given chaos region, a steady equilibrium can be sustained by continuously supplementing the chaos region with new particles with zero average velocity. Thus the total average velocity of all particles in the chaos region may be given by

$$\bar{V}_z' = \frac{\alpha}{\beta}\left[1 - \exp(-\beta t')\right]. \tag{10}$$

In particular, a steady average velocity $\bar{V}_s' \equiv \bar{V}_z'|_{t' \to \infty} = \alpha/\beta$ can be reached when $t' \to \infty$. On the other hand, in the steady equilibrium the Ohm's law leads to

$$\bar{V}_s' = \frac{M_A}{\nu_{\mathrm{eff}}'} \Rightarrow \nu_{\mathrm{eff}}' = \frac{\beta}{\alpha} M_A, \tag{11}$$

where $\nu_{\mathrm{eff}}' = \nu_{\mathrm{eff}}/\omega_c$ is the dimensionless effective collision frequency. The corresponding chaos-induced resistivity η_{eff} is

$$\eta_{\mathrm{eff}} = \frac{m}{n_0 e^2}\nu_{\mathrm{eff}} = \frac{B_0}{e n_0}\nu_{\mathrm{eff}}'. \tag{12}$$

In simulations, 2×10^5 particles are initially selected and distributed uniformly in the region $(-1.0 < x',\ y' < 1.0,\ z' = 0)$ for the X-type magnetic configuration and in the region $(-5.0 < x' < 5.0, -1.0 < y' < 1.0, z' = 0)$ for the double Y-type magnetic configuration. These particles have an initially isotropic Maxwell velocity distribution, i.e.,

$$f(v) = \left(\frac{1}{\sqrt{\pi} v_T}\right)^3 \exp\left(-\frac{v^2}{v_T^2}\right), \tag{13}$$

where $v_T = 0.3 v_A$ is a thermal velocity. By using the Runge-Kutta method with an adaptive time step (the initial step $\delta t' = 0.01$) (Press et al. 1992), we can trace the particles in the chaos region based on the motion Equation (7) and calculate their "average" acceleration α in Equation (8) and the relative escape rate β in Equation (9). Then, the corresponding effective collision frequency ν_{eff}' and the chaos-induced resistivity η_{eff} can be obtained from Equations (11) and (12), respectively.

3 RESULTS AND DISCUSSION

3.1 The Case of in X-type Magnetic Configuration with $l = 0$

Figure 1 shows the X-type magnetic field configuration, where R_c is the radius of chaos region (i.e., the shadow area in the $x - y$ plane) in the unit of $R_0 = \lambda_c$. The guide field B_z and the acceleration electric field E_z are normalized by the reconnection field B_0 and the Alfvénic induced field $v_A B_0$, respectively. For the given chaos

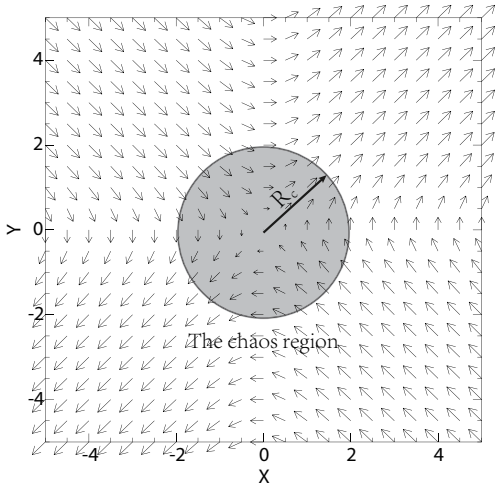

Fig. 1 The X-type magnetic configuration and the chaos region (i.e., shadow area), where R_c is the radius of the chaos region.

region radius $R_c/R_0 = 1.0$ and three fixed values of the acceleration electric field $E'_z = M_A = 0.0001$, 0.0005, and 0.001, the "average" acceleration α, the relative escape rate β, and the effective collision frequency $\nu'_{\rm eff}$ versus the guide field B_z from 0 to $2.0B_0$ are displayed in panels (a), (b), and (c) of Figure 2, respectively, where the parameters α and β are obtained by means of fitting the average velocity along the z axis and the number of the particles surviving inside the chaos region based on Equations (8) and (9), respectively, and $\nu'_{\rm eff}$ is obtained from Equation (11).

From Figure 2(a), the "average" acceleration α increases with the acceleration electric field (i.e., M_A), implying that the acceleration of electrons is dominated by the acceleration electric field in the presence of the guide field, as expected by previous works (Wan et al. 2008; Huang et al. 2010; Wang et al. 2017; Lu et al. 2018; Xia & Zharkova 2018). Figure 2(b) shows that the relative escape rate β also increases with the parameter M_A because the larger acceleration electric field possibly leads to particles escaping more quickly from the chaos region. For the lower guide field case of $B_z/B_0 < 1$, the relative escape rate β decreases considerably as the guide field increases, as shown in Figure 2(b). This is probably because the guide field can effectively prevent particles from escaping from the given chaos region. However, the effect of the guide field on the particle escaping is significantly weakened when the guide field is stronger than the reconnection field, that is, $B_z > B_0$. Figure 2(c) gives the effective collision frequency $\nu'_{\rm eff}$, which has been calculated by Equation (11). As expected by the proportional relation in Equation (11), the parameter $\nu'_{\rm eff}$ in Figure 2(c) has similar changes to the parameter β in Figure 2(b).

Figure 3 displays the same parameters as Figure 2 but for the fixed guide field $B_z = 0.5B_0$ and varying the chaos

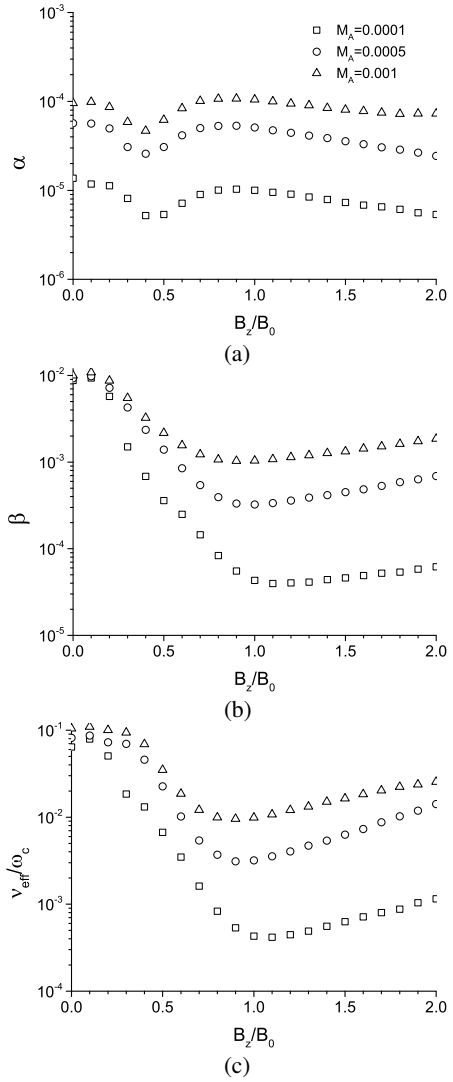

Fig. 2 The "average" acceleration α, the relative escape rate β, and the effective collision frequency $\nu'_{\rm eff}$ versus the guide field B_z in different acceleration electric fields with $M_{\rm A} = 0.0001, 0.0005$, and 0.001.

region radius R_c from 0.1 to $2.0R_0$. From Figure 3, it can be found that the parametric variation in smaller chaos regions of $R_c < R_0$ are considerably different from that in larger regions of $R_c > R_0$. For the smaller regions of $R_c < R_0$, the "average" acceleration α increases with the region radius R_c, the relative escape rate β is nearly a constant, and hence the effective collision frequency $\nu'_{\rm eff}$ decreases with the chaos region radius R_c. For the larger regions of $R_c > R_0$, on the other hand, the "average" acceleration α and the relative escape rate β both decreases with the region radius R_c, but the effective collision frequency $\nu'_{\rm eff}$ increases with the chaos region radius R_c.

For the parameters used in the present simulation, we have $R_0 = v_A/\omega_c = (v_A/v_T)\, r_L \simeq 3.3 r_L$, where $r_L = v_T/\omega_c$ is the cyclotron radius of particles. The Larmor

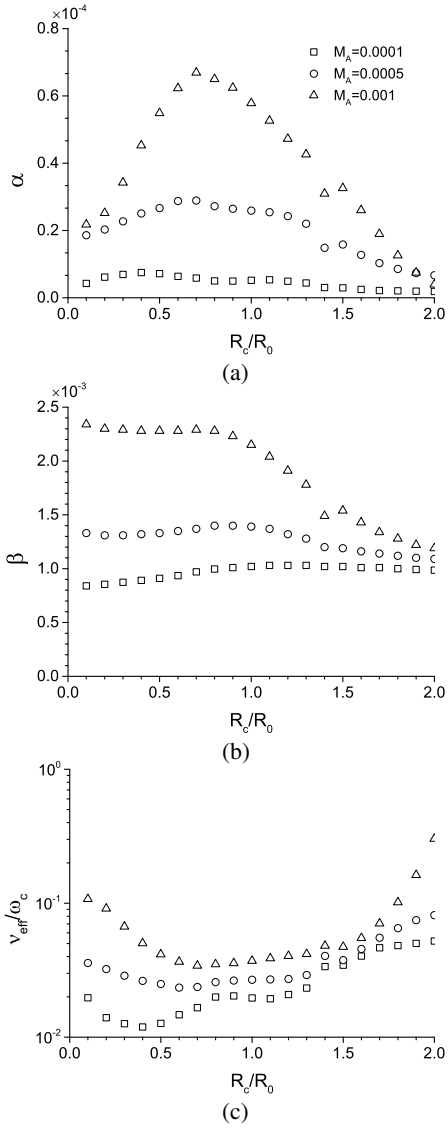

Fig. 3 The "average" acceleration α, the relative escape rate β, and the effective collision frequency $\nu'_{\rm eff}$ versus the chaos region radius R_c/R_0 in different acceleration electric fields with $M_{\rm A} = 0.0001, 0.0005$, and 0.001.

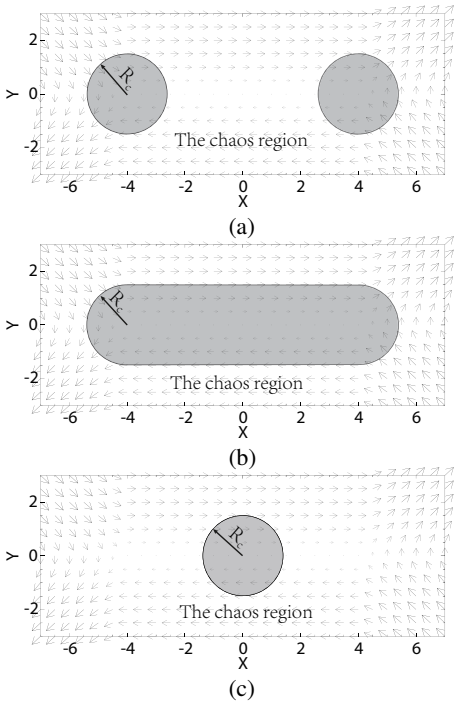

Fig. 4 The double Y-type magnetic configuration and three types of chaos regions denoted by shadow areas, where R_c is the chaos region radius.

cyclotron effect of particle motion due to the Lorentz force generally influences the acceleration and escape processes of the particles in the larger magnetized regions of $R_c > R_0$, which size is considerably larger than the particle cyclotron radius. However, the Larmor cyclotron motion of particles has little effect on their acceleration and escape in the smaller unmagnetized region of $R_c < R_0$ because the size of their moving region is less than the cyclotron radius. In the unmagnetized region of $R_c < R_0$, the "average" acceleration α increases with R_c because the particles have longer effective acceleration times for the larger chaos region. While in the magnetized region of $R_c > R_0$ the acceleration and escape of more particles are hindered by the cyclotron motion for the more chaos region so that the "average" acceleration α and the escape rate β decrease with R_c.

On the other hand, the distribution of the effective collision frequency $\nu'_{\rm eff}$ in Figure 3(c) indicates that the chaos-induced resistivity has an inhomogeneous distribution in the reconnection region, in which the chaos-induced resistivity is higher inside the unmagnetized region of $R_c < R_0$ and outside the magnetized of $R_c > R_0$, but lower in the transition region of $R_c \sim R_0$. In addition, the variation of the effective collision frequency $\nu'_{\rm eff}$ with the acceleration electric field, as shown in Figure 2(c) and Figure 3(c), implies the nonlinear characteristic of the Ohm's law associated with the chaos-induced resistivity, which may be attributed to the influence of the acceleration electric field on the chaos dynamics of the particles and hence on the chaos-induced resistivity in the reconnection region.

3.2 The Case of in Double Y-type Magnetic Configuration with $l = 8$

The double Y-type magnetic configuration is shown in Figure 4, which includes two Y-type magnetic neutral points at $x \pm l/2$ and $y = 0$ and a magnetic neutral line at $y = 0$, and the later denotes a current sheet with a width $l = 8$. The three typical chaos regions are displayed by the shadow areas in panels (a), (b), and (c) of Figure 4, respectively, in which the shadow area in panel (a) displays

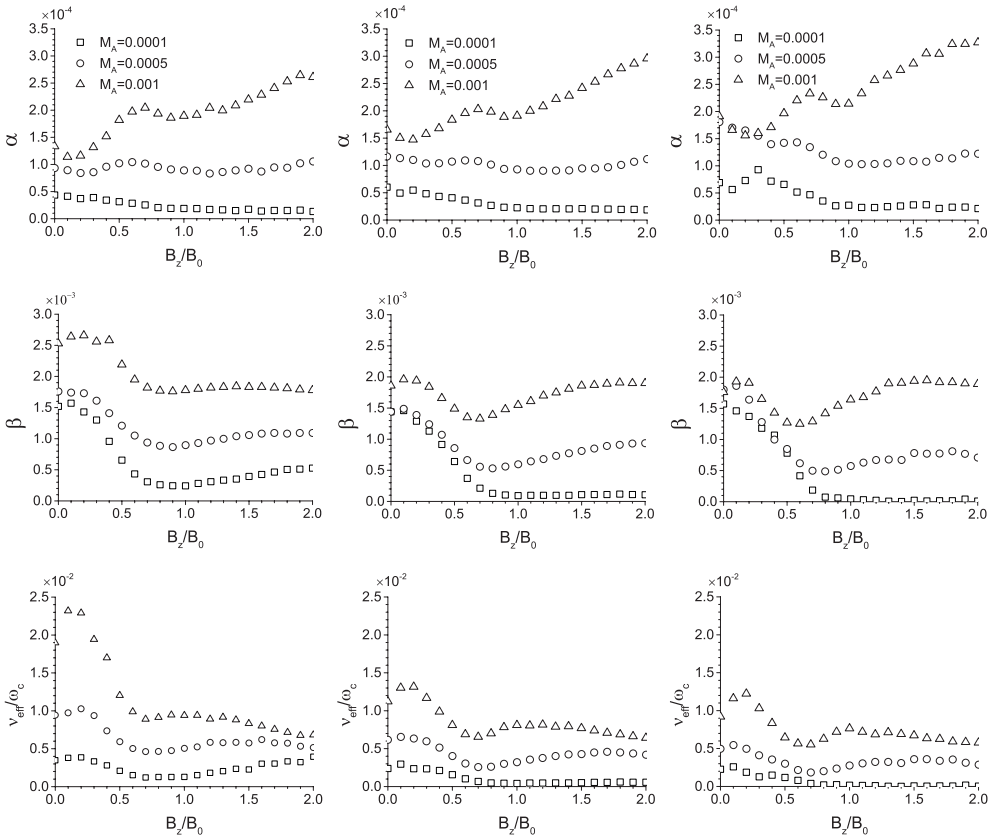

Fig. 5 The "average" acceleration α, the relative escape rate β, and the effective collision frequency $\nu'_{\rm eff}$ versus the guide field B_z for the given chaos region radius $R_c = 1.0R_0$ and three fixed acceleration electric fields $M_A = 0.0001$, 0.0005, and 0.001. The left, middle and right columns present the results of the chaos regions (a), (b), and (c) in Figure 4, respectively.

the chaos regions around the Y-type neutral points (at $x \pm l/2$, $y = 0$), the shadow area in panel (c) does the typical chaos region in the neutral current sheet (at $x = 0$, $y = 0$), and the shadow area in panel (b) contains the whole reconnection current sheet.

Figure 5 plots the "average" acceleration α, the relative escape rate β, and the effective collision frequency $\nu'_{\rm eff}$ versus the guide field B_z for three fixed values of the acceleration electric field $M_A = 0.0001$, 0.0005, and 0.001 and the given chaos region radius $R_c = 1.0R_0$, in which the left, middle, and right columns are corresponding to the chaos regions in panels (a), (b), and (c) of Figure 4, respectively. It is similar to the case of the X-type magnetic configuration presented in Figure 2 that the "average" acceleration α, the relative escape rate β, and the effective collision frequency $\nu'_{\rm eff}$ all increase with the acceleration electric field M_A. Moreover, for the stronger acceleration electric field of $M_A = 0.001$, α increases considerably with the guide field B_z, which is different from that of the X-type magnetic configuration and further confirms that the presence of the guide field will be favorable to the particle acceleration by the acceleration electric field in the reconnection current sheet (Wan et al. 2008; Huang et al. 2010; Wang et al. 2017; Lu et al. 2018; Xia & Zharkova 2018).

In particular, it is worth noticing that the "average" acceleration α and the relative escape rate β increases and decreases, respectively, in turn from left to right columns. As expected by Equation (11), this directly results in the effective collision frequency $\nu'_{\rm eff}$ (or i.e., the corresponding chaos-induced resistivity) in the neutral current sheet chaos region in Figure 4(c) significantly lower than that in the Y-type chaos regions shown in Figure 4(a) and much less than that in the X-type chaos region presented in Figure 1 and Figure 2(c). One of the possible reasons is the particle motion near the X-type neutral point getting into a chaotic orbit more easily (Shang et al. 2017).

For the given guide field $B_z = 0.5B_0$, Figure 6 presents the "average" acceleration α, the relative escape rate β, and the effective collision frequency $\nu'_{\rm eff}$ versus the chaos region radius R_c for the three fixed values of the acceleration electric fields $M_A = 0.0001$, 0.0005, and 0.001, in which the left, middle and right columns are corresponding to the calculation results from the chaos regions (a), (b), and (c) in Figure 4, respectively. From Figure 6, it can be found that the "average" acceleration

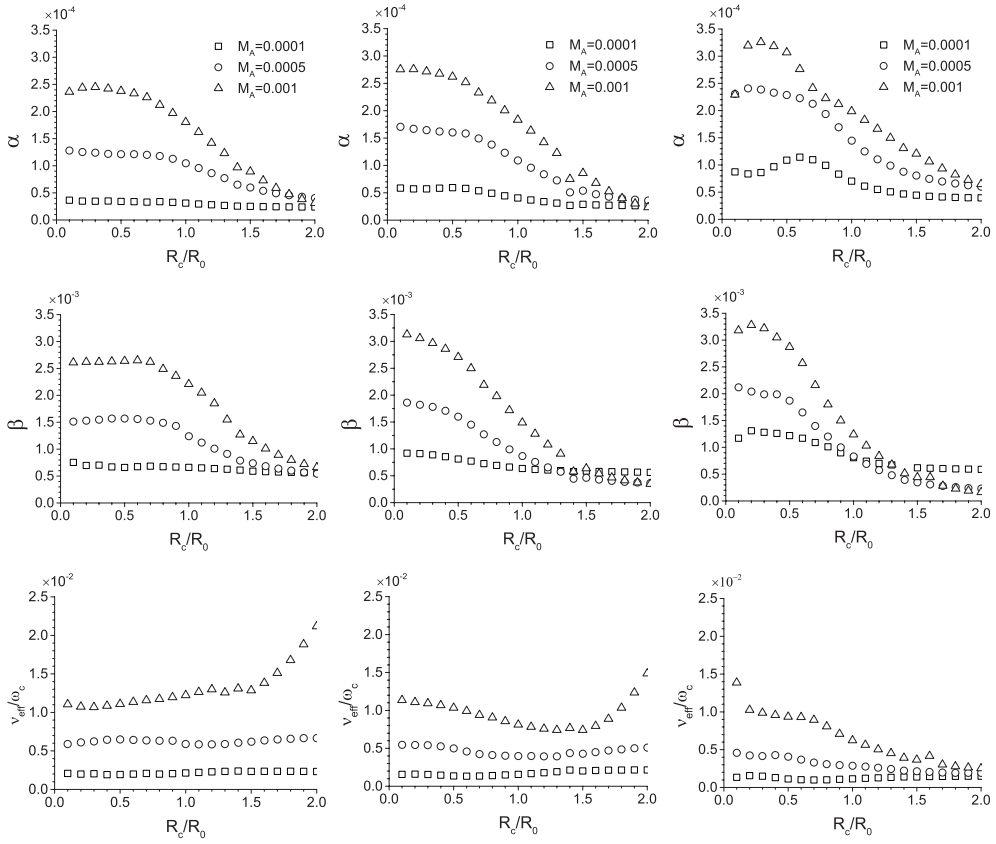

Fig. 6 The "average" acceleration α, the relative escape rate β, and the effective collision frequency $\nu'_{\rm eff}$ versus the chaos region radius R_c for the given guide field $B_z = 0.5B_0$ and three fixed acceleration electric fields $M_A = 0.0001$, 0.0005, and 0.001. The left, middle and right columns present the results of the chaos regions (a), (b), and (c) in Figure 4, respectively.

α and relative escape rate β are determined mainly by the acceleration electric field M_A and are little influenced by the radius R_c in the unmagnetized region of $R_c < R_0$. In the magnetized region of $R_c > R_0$, however, α and β both decrease considerably as the radius R_c increases because the cyclotron motion due to the reconnection field can depress the acceleration and escape of the particles.

Meanwhile, Figure 6 shows that the "average" acceleration α in the central chaos region of the neutral current sheet (in the right column) is higher than that in the Y-type chaos regions (in the left column), similar to Figure 5. However, different from Figure 5, the relative escape rate β in the central chaos region is higher than that in the Y-type chaos regions for the unmagnetized case ($R_c < R_0$) but lower for the magnetized case ($R_c > R_0$). This implies that the particles escape more easily from the unmagnetized region along the parallel reconnection field lines in the current sheet, but more difficultly from the magnetized region due to the hindrance of the cyclotron motion. Moreover, Figure 6 also shows that the effective collision frequency $\nu'_{\rm eff}$, and hence the chaos-induced resistivity, in the Y-type chaos regions (on the left column) is considerably higher than that in the central chaos region of the reconnection current sheet (on the right column), especially for the magnetized region of $R_c > R_0$ and the stronger acceleration electric field M_A.

In addition, it is also worth noticing that the effective collision frequency $\nu'_{\rm eff}$ increases and decreases with the chaos region radius R_c in the Y-type chaos region and in the central chaos region, respectively. It has a potential importance of understanding the dynamics of reconnection current sheets that there are considerably different chaos-induced resistivity in the different types of chaos regions in reconnection current sheets. A lot of investigations have shown that an initial reconnection current sheet with the double Y-type magnetic configuration usually is unstable against the resistive tearing mode, especially in high-temperature plasmas such as the solar corona (Sato 1979; Ugai 1984; Schumacher & Kliem 1996; Nitta 2007; Ma et al. 2015, 2018; Wang et al. 2017; Lu et al. 2018; Xia & Zharkova 2018). This may lead to the formation of a magnetic island, which has an O-type neutral point at its center and two X-type neutral points at its two sides, between the two Y-type neutral points, and then the magnetic island further collapses to a new current sheet with the double Y-type configuration. In consequence,

the development of this instability possibly leads to the occurrence of a island chain with alternate O-type and X-type neutral points. In general, the particle motion near the O-type and X-type neutral points can have significantly different characteristics (Fu et al. 2006).

In the present simplified model, the magnetic island and O-type neutral point can be represented by the central chaos region (i.e., shadow area in Fig. 4(c)) and the central point (at $x = 0$, $y = 0$) in the reconnection current sheet, respectively. The evolution processes of the reconnection current sheet mentioned above, in general, are accompanied by the locally enhancements of the current density at the O-type neutral points and of the dissipation at the X-type neutral points, respectively (Schumacher & Kliem 1996). While the locally enhancements of the current density at the O-type neutral points and of the dissipation at the X-type neutral points indicate that the reduction and the rise of the chaos-induced resistivity (i.e. the anomalous resistivity) in the O-type chaos regions and the X-type chaos regions, respectively. Also this is consistent with the expected results of the effective collision frequency shown in Figures 3 and 6 (see further discussions of the chaos-induced resistivity in the next subsection).

3.3 Possible Application in Solar Coronal Plasmas

It is believed extensively that solar flares are produced by magnetic field reconnections in the solar corona. From Equations (11) and (12), the effective collision frequency due to the effect of the particle orbit chaos can be calculated by

$$\nu_{\rm eff} = \nu'_{\rm eff}\omega_c = \frac{eB_0}{m}\nu'_{\rm eff}, \tag{14}$$

and the corresponding chaos-induced resistivity may be given by

$$\eta_{\rm eff} = \frac{m}{n_0 e^2}\nu_{\rm eff} = \frac{B_0}{en_0}\nu'_{\rm eff}. \tag{15}$$

For typical parameters of pre-flaring coronal plasmas, such as plasma density $n_0 = 10^{16}$ m^{-3}, temperature $T = 500$ eV, and magnetic field $B_0 = 100$ G, Table 1 shows the weighted average of the effective collision frequencies over the chaos region radius R_c from $R_c = 0.1R_0$ to $R_c = 1.0R_0$ for the unmagnetized case,

$$\bar{\nu}'_{\rm eff} \equiv \sum_{r_c=0.1}^{1.0} r_c^2 \nu'_{\rm eff}(r_c) \left(\sum_{r_c=0.1}^{1.0} r_c^2 \right)^{-1}, \tag{16}$$

and from $R_c = 1.1R_0$ to $R_c = 2.0R_0$ for the magnetized case,

$$\bar{\nu}'_{\rm eff} \equiv \sum_{r_c=1.1}^{2.0} r_c^2 \nu'_{\rm eff}(r_c) \left(\sum_{r_c=1.1}^{2.0} r_c^2 \right)^{-1}, \tag{17}$$

where $r_c \equiv R_c/R_0$, r_c^2 is proportional to the number of particles inside the radius R_c and represents the weight of the region with the radius R_c. For the sake of comparison, Table 1 also presents the ratio of the corresponding average chaos-induced resistivity to the classical Spitzer resistivity due to the Coulomb collision, $\eta_{\rm eff}/\eta_{\rm cal}$, where the average chaos-induced resistivity is given by $\eta_{\rm eff} = (B_0/en_0)\,\bar{\nu}'_{\rm eff}$ and the classical Spitzer resistivity $\eta_{\rm cal}$ for the above typical parameters of pre-flaring coronal plasmas can be estimated approximately as 4.65×10^{-8} $(\Omega \cdot {\rm m})$ by the Spitzer formula (Spitzer 1956) with the Coulomb logarithm $\ln\Lambda \approx 10$.

In Table 1, the four types of chaos regions shown in Figure 1, Figure 4(a), Figure 4(b), and Figure 4(c) are denoted by "X-type", "Y-type", "S-type", and "O-type", respectively, and each chaos region is divided into unmagnetized ($R_c < R_0$) and magnetized ($R_c > R_0$) cases, where the three acceleration electric fields $M_A = 0.0001$, 0.0005, and 0.001 have also been used. From Table 1, one can find that in a high-temperature plasma such as the pre-flare coronal plasmas, the chaos-induced resistivity can produce an effective resistivity much higher than the classic collisional resistivity by $5 - 7$ orders of magnitude, implying that the chaos-induced indeed may provide an efficient mechanism for the anomalous resistivity in collisionless reconnection regions (Shang et al. 2017).

However, as shown in Section 3.2, the chaos-induced resistivity can have remarkably different values in the different chaos regions of the reconnection current sheet. For a high-temperature plasma such as the pre-flare coronal plasma, the results of Table 1 show that the chaos-induced resistivity in the X-type chaos region, in general, is significantly higher than that in the O-type chaos region by one to two orders of magnitude. For instance, from Table 1 it can be found that for the magnetized case with a stronger acceleration electric field $M_A = 0.001$, the ratio of the chaos-induced resistivity to the classical Spitzer resistivity, $\eta_{\rm eff}/\eta_{\rm cal}$, in the X-type chaos region is $\sim 1.54 \times 10^7$ remarkably larger than $\sim 4.63 \times 10^5$ in the O-type chaos region by a factor ~ 33. This inhomogeneity of the chaos-induced resistivity in spatial distribution in reconnection current sheets may be attributed to the fact that the particle motion near the X-type neutral point, in general, gets into the chaotic orbits more easily than that near the O-type neutral point (Shang et al. 2017).

In fact, some investigations of dynamic current sheets (Schumacher & Kliem 1996) also suggested that dynamical processes of reconnection current sheets have strongly local dependence, in which the enhanced current channels are formed mainly near the O-type neutral points and the major energy dissipation occurs around the X-type neutral points. While the current enhancement near the O-type neutral point usually implies that there is a lower anomalous resistivity in the O-type chaos region and the dissipation enhancement around the X-type neutral

Table 1 The average effective collision frequency $\bar{\nu}'_{\rm eff}$ and the radio of the chaos-induced to the classical Spitzer resistivity $\eta_{\rm eff}/\eta_{\rm cal}$ for given acceleration electric field $M_A = 0.0001$, 0.0005, and 0.001 in different chaos regions, where "X-type", "Y-type", "S-type", and "O-type" stand for the chaos regions shaded in Figure 1, Fig. 4(a), 4(b), and 4(c), respectively, and the typical parameters of pre-flaring coronal plasmas have been used in the calculation of the classical Spitzer resistivity.

		$\bar{\nu}'_{\rm eff}$			$\eta_{\rm eff}/\eta_{\rm cal}$		
M_A		0.0001	0.0005	0.001	0.0001	0.0005	0.001
X-type	unmagnetized	0.01789	0.02585	0.03835	2.41×10^6	3.47×10^6	5.15×10^6
	magnetized	0.04105	0.05504	0.11460	5.51×10^6	7.39×10^6	1.54×10^7
Y-type	unmagnetized	0.00205	0.00624	0.01175	2.75×10^5	8.38×10^5	1.58×10^6
	magnetized	0.00234	0.00637	0.01594	3.14×10^5	8.55×10^5	2.14×10^6
S-type	unmagnetized	0.00146	0.00427	0.00906	1.96×10^5	5.73×10^5	1.22×10^6
	magnetized	0.00206	0.00461	0.00999	2.77×10^5	6.19×10^5	1.34×10^6
O-type	unmagnetized	0.00110	0.00324	0.00784	1.47×10^5	4.35×10^5	1.05×10^6
	magnetized	0.00143	0.00211	0.00345	1.92×10^5	2.83×10^5	4.63×10^5

point generally implies that there is a higher anomalous resistivity in the X-type chaos region. Therefore, the present results proposes that the chaos-induced resistivity can be responsible for the generation mechanism of the anomalous resistivity that meets the requirements of the dynamics of the reconnection current sheets well.

The inhomogeneity of the chaos-induced resistivity in the reconnection current sheet manifests not only in the difference among various chaos regions but also in the distinction between the magnetized and unmagnetized cases in the same chaos region. From Table 1, for the same chaos region, especially the X-type chaos region with higher chaos-induced resistivity, the chaos-induced resistivity of the magnetized case is considerably higher than that of the unmagnetized case, except for the two cases of the O-type chaos region with a stronger acceleration electric field of $M_A = 0.0005$ and 0.001. This indicates that the cyclotron motion of charged particles in the magnetized case may also contribute to the increase of the chaos-induced resistivity.

In addition, it should be pointed out that the acceleration electric field also can significantly influence the chaos-induced resistivity. The generation and role of the acceleration electric field in the dynamical evolution of reconnection current sheets has been a complex problem (Wang et al. 2017; Lu et al. 2018). In general, the electric field in the reconnection current sheet can be created locally by a magnetic induced process (i.e., $\nabla \times \mathbf{E} = -\partial \mathbf{B}/\partial t$), such as in the X-type chaos region, or by a flow driven process (i.e., $\mathbf{E} = -\mathbf{v} \times \mathbf{B}$), such as in the O-type chaos region. This indicates that there also can be an inhomogeneous electric field in the reconnection current sheet. In particular, the electric field, in general, is greatly dynamical evolution dependent on the dynamical proceeding of the reconnection current sheet. In fact, the present results also show that the chaos-induced resistivity can have considerable variation when the acceleration electric field varies because the electric field may greatly influence the chaotic motion of charged particles. Therefore, the electric field is possibly an important uncertain factor in the dynamics of the reconnection current sheet and more further investigations are needed. Moreover, not all acceleration effects can be included by an equivalent "acceleration electric field" although the electric field possibly plays the most important role in the acceleration (Wang et al. 2017; Lu et al. 2018).

4 SUMMARY AND CONCLUSIONS

The anomalous resistivity has been an open problem in the collisionless magnetic reconnection, which is commonly believed to be responsible for the magnetic energy releasing mechanism of solar flares. Investigations on the dynamics of reconnection current sheets (Sato 1979; Ugai 1984; Schumacher & Kliem 1996; Nitta 2007; Ma et al. 2015, 2018; Wang et al. 2017; Lu et al. 2018; Xia & Zharkova 2018) showed that the dynamical process has remarkably localized and inhomogeneous characteristics, in which the enhancements of current and dissipation occurs, respectively, near the O-type and the X-type neutral points in the reconnection current sheet. In particular, this implies that the anomalous resistivity should have an inhomogeneous distribution in the reconnection current sheet, and hence that a reasonable generation mechanism for the anomalous resistivity should could lead to higher and lower anomalous resistivity near the O-type and X-type neutral points, respectively.

In the present work, the chaos-induced resistivity has been investigated for different magnetic configurations, which may be corresponding to different regions of reconnection current sheet. The present results show that for the case of high-temperature plasmas, such as in the pre-flare coronal plasmas, the chaos-induced resistivity can be much higher than the classic collisional resistivity by a factor $\sim 10^5 - 10^7$. This indicates it to be possible that the chaos-induced resistivity provides an enough high anomalous resistivity for the fast magnetic energy release in solar flares. In particular, the dependence of the chaos-induced resistivity on the magnetic configuration reveals that the chaos-induced resistivity has a greatly inhomogeneous distribution in reconnection current sheets, in which, as

expected by the evolution of dynamical current sheets (Schumacher & Kliem 1996), the chaos-induced resistivity in the X-type chaos region is considerably higher than that in the O-type chaos region of the dynamical current sheet because the particle motion in the X-type chaos region gets into the chaotic orbits more easily than that in the O-type chaos region (Shang et al. 2017). Therefore, the present results proposes that the chaos-induced resistivity can be one of possible candidates for the anomalous resistivity that may meet the requirements of the dynamics of the reconnection current sheets.

As shown in the last section, however, the electric field in the reconnection current sheet can significantly influence the chaos-induced resistivity because the acceleration of particles by the electric field probably can directly affect the chaotic motion of the particles. While usually it is very difficult to determine the distribution of the electric field in the current sheet. In fact, the electric field, the current, and the chaos-induced resistivity can interact each other in the dynamics of the reconnection current sheet, and hence the relationship between them is no longer the linear dependent relation in the common Ohm's law but nonlinear coupling mutually. Therefore, some more self-consistent study is necessary for better understanding of the role of the chaos-induced resistivity in the dynamics of reconnection current sheets. The results by the present simple model proposed that the chaos-induced resistivity may become one of promising mechanisms for the anomalous resistivity in collisionless magnetic reconnection phenomena and deserves to be paid more attention as well as further investigation.

Acknowledgements This work was supported by National Natural Science Foundation of China (Grant Nos. 41531071, 11873018, 11790302 and 11761131007). The authors would like to gratitude to Meng Shang and Xiao-Long Wang for their help in the simulation.

References

Andriyas, T., & Spencer, E. 2014, Journal of Geophysical Research (Space Physics), 119, 4290
Biskamp, D., Schwarz, E., & Drake, J. F. 1995, Phys. Rev. Lett., 75, 3850
Bulanov, S. V., Pegoraro, F., & Sakharov, A. S. 1992, Physics of Fluids B, 4, 2499
Bychenkov, V. Y., Silin, V. P., & Uryupin, S. A. 1988, Phys. Rep., 164, 119
Cai, H. J., & Lee, L. C. 1997, Physics of Plasmas, 4, 509
Carter, T. A., Ji, H., Trintchouk, F., et al. 2002, Phys. Rev. Lett., 88, 015001
Deng, X. H., & Matsumoto, H. 2001, Nature, 410, 557
Dungey, J. W. 1953, Philosophical Magazine, 44, 725
Dungey, J. W. 1961, Phys. Rev. Lett., 6, 47
Fu, X. R., Lu, Q. M., & Wang, S. 2006, Physics of Plasmas, 13, 012309
Furth, H. P., Killeen, J., & Rosenbluth, M. N. 1963, Physics of Fluids, 6, 459
Gekelman, W., Vincena, S., Van Compernolle, B., et al. 2011, Physics of Plasmas, 18, 055501
Giovanelli, R. G. 1946, Nature, 158, 81
Grad, H., & Norton, R. V. 1962, Nuclear Fusion Suppl, 1, 61
Huang, C., Lu, Q., & Wang, S. 2010, Physics of Plasmas, 17, 072306
Huba, J. D., Drake, J. F., & Gladd, N. T. 1980, Physics of Fluids, 23, 552
Kim, E.-j., & Diamond, P. H. 2001, ApJ, 556, 1052
Lazarian, A., Eyink, G. L., Jafari, A., et al. 2020, Physics of Plasmas, 27, 012305
Lazarian, A., & Vishniac, E. T. 1999, ApJ, 517, 700
Liu, Y.-H., Daughton, W., Karimabadi, H., et al. 2013, Phys. Rev. Lett., 110, 265004
Lu, Q., Wang, H., Huang, K., et al. 2018, Physics of Plasmas, 25, 072126
Lyutikov, M. 2006, MNRAS, 369, L5
Ma, Z. W., Chen, T., Zhang, H. W., & Yu, M. Y. 2018, Scientific Reports, 8, 10521
Ma, Z. W., Wang, L. C., & Li, L. J. 2015, Physics of Plasmas, 22, 062104
McPherron, R. L. 1979, Reviews of Geophysics and Space Physics, 17, 657
Nitta, S.-y. 2007, ApJ, 663, 610
Numata, R., & Yoshida, Z. 2002, Phys. Rev. Lett., 88, 045003
Numata, R., & Yoshida, Z. 2003, Phys. Rev. E, 68, 016407
Parker, E. N. 1957, Physical Review, 107, 830
Press, W. H., Teukolsky, S. A., Vetterling, W. T., et al. 1992, Numerical recipes in FORTRAN, The Art of Scientific Computing (Cambridge: Univ. Press, —c1992, 2nd ed.)
Sato, T. 1979, J. Geophys. Res., 84, 7177
Schmidt, G. 1962, Physics of Fluids, 5, 994
Schumacher, J., & Kliem, B. 1996, Physics of Plasmas, 3, 4703
Shang, M., Wu, D. J., Chen, L., & Chen, P. F. 2017, RAA (Research in Astronomy and Astrophysics), 17, 3
Singh, K. A. P., & Subramanian, P. 2007, Sol. Phys., 243, 163
Spitzer, L. 1956, Physics of Fully Ionized Gases (New York: Interscience Publishers)
Strauss, H. R. 1988, ApJ, 326, 412
Ugai, M. 1984, Plasma Physics and Controlled Fusion, 26, 1549
Voitenko, Y. M. 1995, Sol. Phys., 161, 197
Wan, W., Lapenta, G., Delzanno, G. L., & Egedal, J. 2008, Physics of Plasmas, 15, 032903
Wang, H., Lu, Q., Huang, C., & Wang, S. 2017, Physics of Plasmas, 24, 052113
Xia, Q., & Zharkova, V. 2018, A&A, 620, A121
Yoshida, Z., Asakura, H., Kakuno, H., et al. 1998, Phys. Rev. Lett., 81, 2458